GDCh Research Article Angewandte International Edition Chemie www.angewandte.org

How to cite: Angew. Chem. Int. Ed. 2024, e202412680
doi.org/10.1002/anie.202412680

Electrocatalytic H_2 Oxidation

Dilute Pd–Ni Alloy through Low-temperature Pyrolysis for Enhanced Electrocatalytic Hydrogen Oxidation

Yi Yuan, Xue-Qian Wu, Xi Yin, Heng-Yu Ruan, Ya-Pan Wu, Shuang Li, Guangtong Hai, Gaixia Zhang, Shuhui Sun,* and Dong-Sheng Li**

Abstract: Designing highly active and cost-effective electrocatalysts for the alkaline hydrogen oxidation reaction (HOR) is critical for advancing anion-exchange membrane fuel cells (AEMFCs). While dilute metal alloys have demonstrated substantial potential in enhancing alkaline HOR performance, there has been limited exploration in terms of rational design, controllable synthesis, and mechanism study. Herein, we developed a series of dilute Pd–Ni alloys, denoted as *x* % Pd–Ni, based on a trace-Pd decorated Ni-based coordination polymer through a facile low-temperature pyrolysis approach. The *x*% Pd–Ni alloys exhibit efficient electrocatalytic activity for HOR in alkaline media. Notably, the optimal 0.5 % Pd–Ni catalyst demonstrates high intrinsic activity with an exchange current density of 0.055 mA cm^{-2}, surpassing that of many other alkaline HOR catalysts. The mechanism study reveals that the strong synergy between Pd single atoms (SAs)/Pd dimer and Ni substrate can modulate the binding strength of proton (H)/hydroxyl (OH), thereby significantly reducing the activation energy barrier of a decisive reaction step. This work offers new insights into designing advanced dilute metal or single-atom-alloys (SAAs) for alkaline HOR and potentially other energy conversion processes.

Introduction

Anion-exchange membrane fuel cells (AEMFCs) are recognized as one of the most promising energy conversion devices, facilitating the utilization of clean hydrogen energy and mitigating fossil fuel consumption.[1] The AEMFC system involves two electrode reactions: the oxygen reduction reaction (ORR) at the cathode and the hydrogen oxidation reaction (HOR) at the anode.[2] Despite the rapid development of highly efficient non-noble metal-based cathodic ORR catalysts, the sluggish kinetics of HOR and the high cost associated with anodic catalysts in alkaline media pose challenges to the widespread adoption of AEMFCs.[3] In this context, significant efforts have been dedicated to exploring efficient and cost-effective HOR electrocatalysts from various perspectives.[4] Representative mechanisms like the hydrogen binding energy (HBE), bifunctional, and potential of zero free charge (PZFC) theories, along with typical Tafel-Volmer/Heyrovsky-Volmer reaction pathways of alkaline HOR, highlight that the HOR activity is essentially determined by ads-/desorption of the reaction intermediates, activation energy and reaction energy barrier.[5] Therefore, various strategies, such as geometry, composition, heteroatom-dopping, and substrate engineering, have been proposed to modulate the physical properties and electronic structures of catalysts.[6] Among these strategies, alloying stands out as a prominent method to enhance HOR performance. For instance, Huang et al. reported a subnanometer high-entropy alloy (HEA) nanowire (PtRuNiCoFeMo) as an efficient catalyst for alkaline HOR.[7] The strong synergy among different metals in HEA significantly alters their electronic properties, which eventually regulates the hydrogen and hydroxide binding energies (HBE/OHBE). More recently, Pang et al. demonstrated

[*] Y. Yuan, X. Yin, H.-Y. Ruan, Prof. Dr. Y.-P. Wu, Dr. S. Li, Prof. Dr. D.-S. Li
College of Materials and Chemical Engineering, Key Laboratory of Inorganic Nonmetallic Crystalline and Energy Conversion Materials, China Three Gorges University, Yichang 443002, P. R. China
E-mail: lidongsheng1@126.com

Dr. X.-Q. Wu
College of Electrical Engineering & New Energy, China Three Gorges University, Yichang, 443002, P. R. China
E-mail: wuxueqiansnail@163.com

Dr. G. Hai
Beijing Advanced Innovation Center for Materials Genome Engineering, Beijing Key Laboratory of Function Materials for Molecule & Structure Construction, School of Materials Science and Engineering, University of Science and Technology Beijing, Beijing 100083, P. R. China

Prof. Dr. G. Zhang
Department of Electrical Engineering, École de Technologie Supérieure (ÉTS), Montréal, Québec H3C 1K3, Canada

Prof. Dr. S. Sun
Institut National de la Recherche Scientifique (INRS), Center Energy, Materials and Telecommunications, Varennes, Québec J3X 1P7, Canada
E-mail: shuhui.sun@inrs.ca

that the alloying effect in RuCoPt can influence the electronic structure of Ru atoms, which results in optimal adsorption strength of reaction intermediates and accelerated HOR kinetics.[8] Despite the considerable potential of alloy catalysts (e.g. PtPd, PtNi, PdCu, AuPd, AuPt, etc.),[9] the multimetallic components and unpredictable atom ensemble configurations unavoidably elevate element costs and complicate the optimization of HOR performance.

Currently, dilute metal alloys or single-atom-alloys (SAAs) represent a compelling strategy for maximizing both economic benefits and optimized properties, due to their efficient atom utilization and well-defined binding environments.[10] For alkaline HOR, the conventional alloy catalysts face limitations imposed by the linear scaling relationship between activation energy and reaction energy (Brønsted-Evans-Polanyi (BEP) relation), impeding further performance improvement. Intriguingly, dilute alloys or SAAs offer the potential to break these constraints, as they decouple adsorption energy from site-binding preferences.[10c,11] This unique advantage enables dilute alloys or SAAs as catalysts with exceptional properties for various energy conversion processes, including water splitting (HER/OER),[10d,12] oxygen reduction reaction (ORR),[13] and methanol oxidation reaction (MOR).[14] However, the targeted design of metal alloys with atomically dispersed collaborative elements specifically for HOR applications has rarely been reported. Meanwhile, a majority of existing HOR SAA or dilute alloy catalysts, such as $RuNi_1$/NCs,[15] Mo–Pt/NC,[5d] $PtPdCu_1$/C,[9d] Ln_1Pt/NCs,[16] Ru_1Pt_n-SAA,[17] and $(Pt_{0.9}Pd_{0.1})_3Fe$,[18] were fabricated using noble metals as host materials to anchor single atoms, leaving room for further cost reduction and exploration of diverse atom ensembles.

Herein, we report a novel method for dispersing Pd atoms in a near-monatomic state into the lattice of metallic Ni, forming structurally clear and stable dilute Pd–Ni alloys (denoted as *x*% Pd–Ni). This achievement is realized through a facile pyrolysis procedure mediated by a Ni-based coordination polymer (NiC_2O_4–CP). The selection of synergistic components in *x*% Pd–Ni was based on the following considerations: (a) Pd, as a Pt-group metal with relatively higher reserves, has a similar electronic structure to Pt and exhibits Pt-like activity; (b) alloying Ni with Pd may modulate both the HBE and OHBE at the Pd/Ni interface, guided by the volcano relationship between HBE/OHBE and metals.[6] The atomic and electronic structural features of *x*% Pd–Ni were confirmed through detailed microscopic and spectroscopic characterizations. Theoretical calculations unveil the charge deviation from Ni to Pd, resulting in a modified electronic structure of two metal sites. Capitalizing on this, the optimal 0.5 % Pd–Ni catalyst exhibits excellent electrocatalytic activity and durability toward HOR in 0.1 M KOH electrolyte, with a mass activity of 4.275 $mA\,mg^{-1}_{metal}$, outperforming that of many other HOR catalysts in alkaline media. By deciphering the HOR process on 0.5 % Pd–Ni, we discovered that the synergy within dilute Pd–Ni alloy overcomes the limitation of the well-known BEP relation in heterogeneous catalysis, thereby boosting the HOR performance. This study not only provides a facile method for the controllable synthesis of dilute metal alloys but also promotes the fundamental understanding of dilute alloys or SAAs for alkaline HOR and other energy conversion processes.

Results and Discussion

The Pd–Ni catalysts were synthesized using a simple solvothermal reaction and pyrolysis method (Scheme 1). First, a crystalline one-dimensional (1D) nickel oxalate coordination polymer (NiC_2O_4-CP, Figure S1) was conveniently synthesized at room temperature, following previously reported literature.[19] Second, vacuum-activated samples of NiC_2O_4-CP were mixed with palladium chloride solution under stirring to form Pd@NiC_2O_4-CP precursor. In the final step, the precursor samples were annealed in an Ar/H_2 atmosphere to produce the target catalysts (Experimental details are presented in the Supporting Information). Powder X-ray diffraction (PXRD) patterns of the intermediate products (Figure S2) and final catalysts were recorded to verify their phase and purity.

As shown in Figure 1a, only three strong diffraction peaks at 44.5, 51.8, and 76.4° are evident in the PXRD patterns of *x*% Pd–Ni samples. These peaks correspond to the (111), (200), and (220) crystal planes of face-centered cubic (*fcc*) Ni (PDF # 04-0508), respectively, affirming that the main substrate of the catalyst is metallic Ni. The presence of the Pd element is not discernible from these peaks, suggesting its coexistence in ultra-low quantities. The chemical states of Ni and Pd elements in the catalysts were elucidated through X-ray photoelectron spectroscopy (XPS) analyses. In the XPS spectra of 0.5 % Pd–Ni, the Ni 2p spectrum shows a $2p_{3/2}$ peak at 855.4 eV and a $2p_{1/2}$peak at 873.4 eV, characteristic of metallic Ni^0 and divalent Ni^{2+}. The latter is presumed to result from the inevitable superficial oxidation of Ni, given its nano-sized feature (Figure 1b).[20] Meanwhile, two extremely weak characteristic peaks assigned to Pd $3d_{3/2}$ (340.8 eV) and Pd $3d_{5/2}$ (335.6 eV) appear in the Pd 3d high-resolution spectrum, confirming the successful introduction of trace Pd^0 species in the catalyst (Figure 1c). The mass percentage of Pd in 0.5 % Pd–Ni is only 0.8 % (mole percent: 0.47 %), as determined by inductively coupled plasma mass spectrometry (ICP-MS). This further confirms the extremely low Pd loading in the

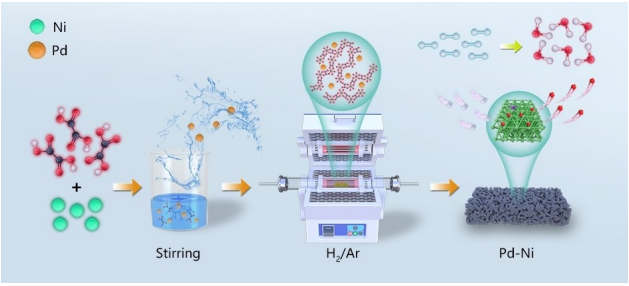

Scheme 1. Schematic diagram of the synthesis route of *x*% Pd–Ni.

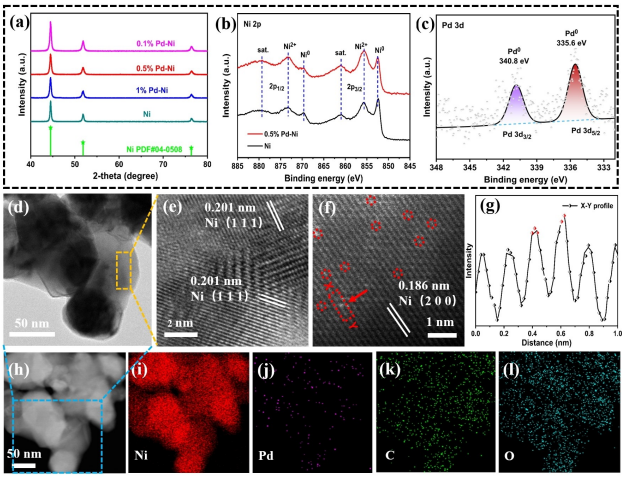

Figure 1. Composition and morphologies of *x*% Pd–Ni catalysts. (a) PXRD patterns of Ni and *x*% Pd–Ni (*x* = 0.1, 0.5, 1). (b, c) XPS spectra of 0.5 % Pd–Ni in (b) Ni 2p and (c) Pd 3d. (d) TEM, (e) HR-TEM, and (f) AC-HAADF-TEM images of 0.5 % Pd–Ni. (g) Intensity profile along the line X–Y in (f) highlighting the atomic dispersion of Pd on the Ni surface. (h–l) HRTEM and elemental mapping images of 0.5 % Pd–Ni.

material, which is consistent with the XPS and PXRD results.

The morphology and microstructure of the as-prepared catalysts were investigated through scanning electron microscopy (SEM) and transmission electron microscopy (TEM). As presented in Figure S3, both the material derived from NiC_2O_4–CP(Ni) and as-prepared 0.5 % Pd–Ni exhibit a coral-like structure composed of homogeneous nanoparticles with a diameter of ~100–200 nm. The TEM and high-resolution (HR) TEM images for 0.5 % Pd–Ni reveal the smooth and clear surface of the Ni substrate, where no Pd nanoparticles or Pd_n clusters can be observed (Figure 1d and Figure S4) (without any nucleation). The lattice fringes of the Ni substrate with an interplanar spacing of 0.20 nm (Figure 1e) can be attributed to the (111) planes of the *fcc* Ni, consistent with PXRD analysis. The corresponding elemental mapping images and X-ray energy dispersive spectroscopy (EDS) of 0.5 % Pd–Ni (Figure h–l and Figure S7) confirm the uniform dispersion of all elements, with Ni dominating at 96.6 wt %. For atomic information on the existence form and location of the Pd species, aberration-corrected high-angle annular dark-field TEM (AC-HAADF-TEM) was conducted. Notably, due to the larger Z value of Pd compared to Ni, several bright spots attributed to Pd SAs (marked with red circles) were found to be anchored on the surface of the (200) planes of the Ni substrate (Figure 1f and Figure S5), as indicated by the intensity profile in Figure 1g and Figure S6. Additionally, the lattice spacing of Ni (200) (0.186 nm) in 0.5 % Pd–Ni is slightly larger than that of the *fcc* Ni (200) facets (0.176 nm), suggesting that Pd atoms partially replaced the crystal lattice Ni atoms, partially forming a Pd–Ni-SAA structure and inducing lattice distortion.

The detailed electronic structures and coordination environments of Pd SAs in 0.5 % Pd–Ni and 1 % Pd–Ni were elucidated through synchrotron-based X-ray absorption near-edge structure spectroscopy (XANES) and extended X-ray absorption fine structure spectroscopy (EXAFS) at the Pd K-edge. The XANES profiles in Figure 2a demonstrate the comparable cationic environment of Pd in 0.5 % Pd–Ni, with the scattering oscillation of the Pd K-edge positioned between Pd foil and PdO references. Notably, for the Pd foil, two distinct characteristic peaks at 24367 and 24391 eV are observed in both 0.5 % Pd–Ni and 1 % Pd–Ni samples, exhibiting a shift to higher energies by about 3–4 eV. This shift implies the high dispersion of Pd atoms and charge transfer between Pd and Ni.

The EXAFS spectrum of 0.5 % Pd–Ni reveals a strong signal of Pd–Ni coordination with a coordination number (CN) of 6.1, while the contribution of Pd–Pd coordination is weak (CN = 1.5) (Figure. 2b, Table 1). This observation further confirms that the majority of Pd atoms are atomically dispersed and the two synergetic metals combine in a dilute alloying state.[20,21,22] Additionally, K-space spectra in Figure 2c indicate no apparent signals of metal-metal bonding at a high k value region for the 0.5 % Pd–Ni sample, suggesting the single-atom state of most Pd. The wavelet transform in Figure 2d supports this conclusion, aligning with the AC-HAADF-TEM observations. Notably, the CN (6.1) of Pd–Ni in 0.5 % Pd–Ni is lower than the average CN (7.8) of Ni–Ni in cuboctahedral Ni NP cluster model reported in the literature.[20,23] When the Pd atoms were uniformly distributed over both the surface and the bulk of Ni host, it is expected that the Pd–Ni CN will be higher than the average CN for surface atoms. This affirms that most of the monoatomic Pd is distributed in the outermost layer of the Ni substrate.[24] With an increase in Pd loading, EXAFS curve fitting for 1 % Pd–Ni shows a decrease in the Pd–Ni CN to 3.6 and an increase in the

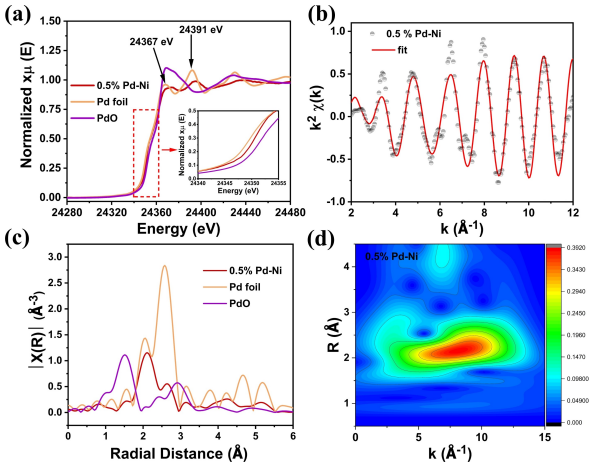

Figure 2. Structural characterization of 0.5 % Pd–Ni catalyst. (a) Pd K-edge XANES spectra of the 0.5 % Pd–Ni sample, Pd foil, and PdO references. (b) Pd K-edge EXAFS (points) and fitting (line) for the sample, shown in k^2 weighted *k*-space. (c) The comparison of Pd K-edge EXAFS, shown in k^2 weighted *R*-space. (d) Corresponding wavelet transform of EXAFS spectra of the Pd K-edge for 0.5 % Pd–Ni.

Table 1: Fitting parameters from the modeling of the EXAFS data collected at the Pd K-edge.

Sample	Shell	CN[a]	R (Å)[b]	σ^2 (Å^2)[c]	ΔE_0 (eV)	S_0^2	R factor
Pd foil	Pd–Pd	12 (set)	2.74	0.007	4.4 ± 0.4	0.9828 (calculated)	0.018
0.5 % Pd–Ni	Pd–Pd Pd–Ni	1.5 ± 0.2 6.1 ± 0.6	2.72 2.63	0.001 0.015	2.8 ± 0.9	0.9828 (set)	0.018
1 % Pd–Ni	Pd–Pd Pd–Ni	3.6 ± 0.1 3.9 ± 0.2	2.72 2. 59	0.006 0.011	2.5 ± 0.3	0.7931 (set)	0.006

[a] coordination number. [b] the distance to the neighboring atom. [c] the Mean Square Relative Displacement (MSRD).

Pd–Pd CN to 3.9 (Figure S8b. S8c and S8d, and Table 1), indicating the emergence of Pd clusters. This process of spreading Pd SAs on the surface of the Ni host is driven by the formation of strong Pd–Ni bonds and the reduction of the surface energy of isolated Pd atoms.

The electrocatalytic properties for HOR of all the x% Pd–Ni ($x = 0.1$, 1, 0.5) catalysts were evaluated in an H_2-saturated 0.1 M KOH electrolyte using a rotating disk electrode (RDE) system. The commercial Pt/C (20 wt %) was chosen as a reference material (additional test details can be found in the Supporting Information). HOR polarization curves for these catalysts obtained by linear sweep voltammetry (LSV) measurement at a rotating speed of 1600 rpm are shown in Figure 3a. Evidently, the x% Pd–Ni series exhibit significantly enhanced hydrogen oxidation currents compared to the Ni sample derived from NiC_2O_4-CP. In particular, the LSV curve of the optimal 0.5 % Pd–Ni catalyst closely aligns with the state-of-the-art Pt/C across the kinetic to the diffusion-limiting regions, achieving a current density of up to 2.2 mA cm^{-2} at an overpotential of 0.1 V. As the rotating speed increases from 400 to 2500 rpm, the anode current density continues to increase due to the acceleration of mass transfer, as presented in Figure 3b. By fitting j^{-1} vs $\omega^{-1/2}$ at an overpotential of 25 mV ($\eta = 25$ mV), a slope of 13.5 cm$^2_{disk}$ mA^{-1} rpm$^{1/2}$ is obtained, which is close to the theoretical value for the two-electron HOR process (14.8 cm$^2_{disk}$ mA^{-1} rpm$^{1/2}$). For the reference samples, 0.1 % Pd–Ni and 1 % Pd–Ni, the slopes are calculated to be 14.68 and 15.64 cm$^2_{disk}$ mA^{-1} rpm$^{1/2}$ (Figure S11), respectively. Furthermore, the kinetic current density (j^k) without interfacial mass transfer is extracted according to the Koutecky–Levich equation coupled with Butler–Volmer (BV) fitting. As shown in Figure 3c, the 0.5 % Pd–Ni exhibits the highest j^k value (7.5 mA cm^{-2} at 50 mV), which is about 6.2 and 6.4 times higher than that of 0.1 % Pd–Ni (1.21 mA cm^{-2}) and 1 % Pd–Ni (1.18 mA cm^{-2}), respectively. The apparent exchange current density (j^0) of these catalysts was further calculated from the micro-polarization region (−5–5 mV) based on the B–V equation (Figure 3d). The obtained j^0 values for x% Pd–Ni catalysts are summarized in Table S3, where the 0.5 % Pd–Ni exhibits the highest HOR activity (1.74 mA cm$^{-2}_{disk}$). After normalization by the electrochemical surface area (ECSA, Figure S12) and catalyst loading, the values of the exchange current densities of 0.5 % Pd–Ni were found to be 0.055 mA cm^{-2} (area activity, $j^{0,s}$) and 4.275 mA mg^{-1} (mass activity, $j^{0,m}$), surpassing most reported Ni-based (Figure 3e) and Pd-based (Figure 3f) HOR catalysts. The intrinsic activity of other representative materials has also been investigated and listed in Tables S4 and S5.

The stability of these electrocatalysts was evaluated through an accelerated durability test (ADT) by conducting 1000 CV measurements in H_2-saturated 0.1 M KOH and Ar-saturated 0.1 M KOH solutions, respectively. As illustrated in Figures 3g and 3 h, the LSV polarization curves of 0.5 % Pd–Ni only show slight attenuation after 1000 CV cycles in the aforementioned electrolytes, and the final exchange current density (j^0) is maintained at 77.2 % and 92.7 %. Given the inevitable presence of CO in hydrogen fuel, the CO tolerance of the catalysts is a crucial factor in determining their practical applications. Therefore, the CO-tolerance assessment of 0.5 % Pd–Ni and other reference materials was conducted through a chronoamperometry test in H_2 gas containing 100 ppm CO-saturated-0.1 M KOH. As observed from the I–T curves, the anodic current density on both 0.5 % Pd–Ni and Pt/C samples gradually decreased during the long-term test. The former catalyst can maintain about 50 % of the initial current density while the latter retains 46 % of the original j^0 (Figure 3i). Additionally, ADT and CO-tolerance tests on 0.1 % Pd–Ni and 1 % Pd–Ni were carried out, indicating that all x% Pd–Ni samples exhibit better stability and CO-tolerance compared to 20 % Pt/C (Figures S13 and S14). To understand the stability origin of HOR and unravel the possible surface structural evolution of 0.5 % Pd–Ni during reactions, we investigated the structural and composition features of the samples post-catalysis using multiple characterization techniques. HR-TEM images and PXRD patterns preliminarily confirmed the well-maintained morphology, clean surface, and crystalline phase of 0.5 % Pd–Ni after electrocatalysis (Figures S15 and S16). Further, results from ICP-MS measurement demonstrated that the 0.5 % Pd–Ni maintains a relatively steady Pd/Ni ratio or mass percentage of Pd after 200/500/1000 CV cycles (Table S6). Since CO is a well-established probe molecule for Pd ensemble structures, we employed in situ CO-DRIFT spectroscopy at 30 °C to monitor the surface structure of the 0.5 % Pd–Ni alloy and its dynamic response to CO in flow mode. As depicted in Figure S17, during CO adsorption/desorption process, the adsorption band at 2171 cm^{-1} corresponds to gaseous CO, while the bands at 2117, 2088, and 1975 cm^{-1} are attributed to linear CO on Pd and bridge-bonded CO, respectively.[25] The different binding configurations of CO (linear and bridge-bonded CO)

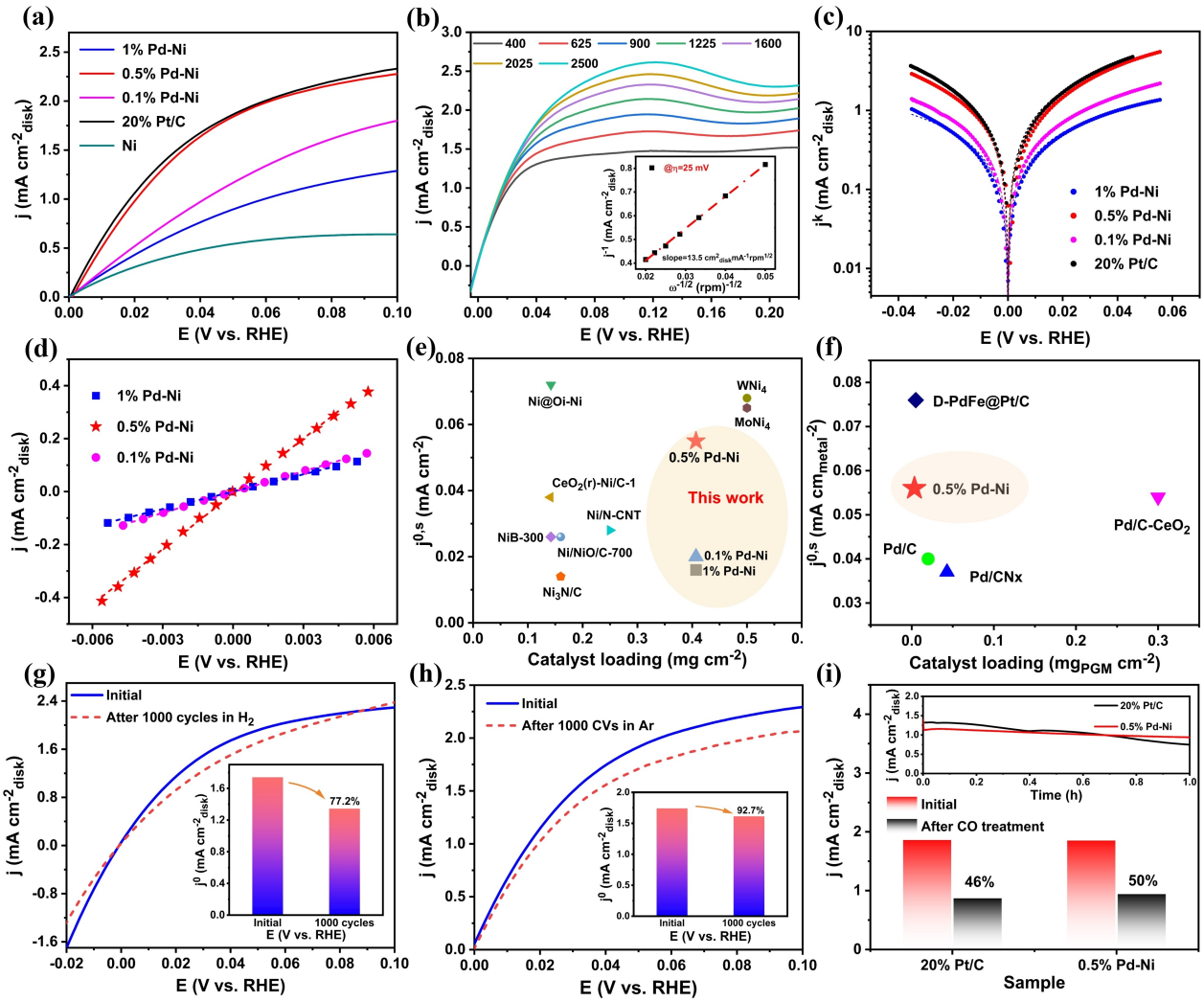

Figure 3. Electrocatalytic alkaline HOR performances. (a) HOR polarization curves of Ni, *x*% Pd–Ni ($x=0.1$, 0.5, 1), and 20% Pt/C in H_2-saturated 0.1 M KOH (Sweep rate: 5 mV s^{-1}; rotation speed: 1600 rpm). (b) polarization curves of 0.5% Pd–Ni at various rotation speeds from 2500 to 400 rpm. The inset shows the Koutecky–Levich plot obtained at an overpotential of 25 mV. (c) Tafel plots of the kinetic current densities. (d) Linear fitting curves in micro-polarization region (−5 to 5 mV). (e/f) Comparisons of $j^{0,s}$ of 0.5% Pd–Ni with that of the other reported Ni-based and Pd-based catalysts. (g/h) LSV polarization curves and exchange current density histogram of 0.5% Pd–Ni in H_2-saturated or Ar-saturated 0.1 M KOH before and after 1000 CV cycles. (i) Chronoamperometry curves of 0.5% Pd–Ni in H_2-saturated 0.1 M KOH containing 100 ppm CO measured at 0.05 V vs RHE and histogram of exchange current density before and after CO treatment.

further confirm the presence of Pd ensembles on the surface of the dilute Pd–Ni alloy catalyst, rather than just Pd SAs, consistent with the findings from AC-HAADF-TEM and EXAFS analyses. The intensity of these characteristic peaks changed synchronously with increasing or decreasing CO coverage, indicating the stability of the surface structure of 0.5% Pd–Ni. Collectively, these findings underscore the significant potential of Pd–Ni dilute alloy in reducing the usage of noble metals for alkaline HOR, without compromising on activity and stability.

To elucidate the HOR reaction mechanism on 0.5% Pd–Ni under alkaline conditions, theoretical calculations based on density functional theory (DFT) were conducted. Considering the structural characterization results of 0.5% Pd–Ni, the Pd atoms are primarily dispersed on the Ni (200) crystal face, forming a dilute Pd–Ni alloy. The Ni (200) surface was chosen to represent pure Ni substrate, and the theoretical models of dilute Pd–Ni alloy were established by introducing a single Pd atom (Pd–Ni) or Pd dimer (Pd_2–Ni) to replace the lattice Ni (Figure 4), respectively. Given that H* and OH* are two key reactive intermediates during the HOR process, the binding energy of H* (HBE) and OH* (OHBE) at different sites was initially evaluated to identify the optimal adsorption configuration. All three models (Ni, Pd–Ni, and Pd_2–Ni alloy) exhibited stronger adsorption strength toward H* and OH* at hollow sites (Figure S18–S21, S25) compared to the top or bridge sites, which showed higher binding energies (Table S7, Figure S22). Interestingly, the determined optimal adsorption sites of H*/OH* within dilute Pd–Ni alloy are located between two lattice Ni atoms adjacent to Pd SA or Pd dimer, similar to that of the pure Ni substrate. This implies that the isolated Pd SA and Pd dimer

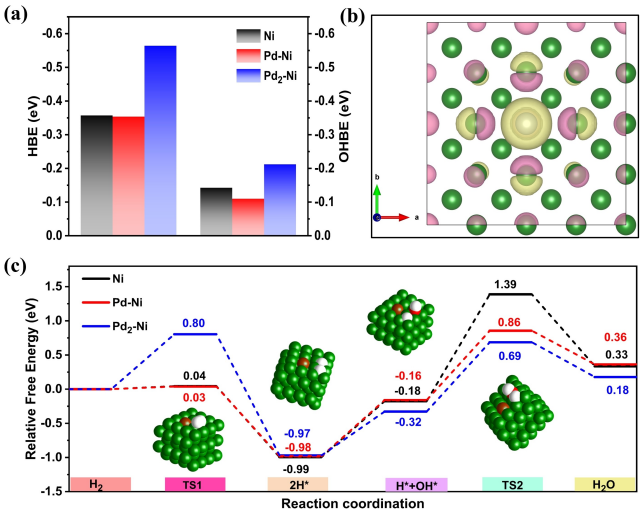

Figure 4. Theoretical calculations and reaction mechanism of alkaline HOR. (a) Calculated HBE and OHBE on the surface of Ni, Pd–Ni, and Pd_2–Ni models. (b) Differential charge density diagram of Pd–Ni (top view). (c) Free energy diagrams of the key intermediates involved in HOR on Ni, Pd–Ni, and Pd_2–Ni surfaces.

appear to be absent in capturing reactive intermediates directly but regulate the electronic structure of neighboring Ni atoms. Comparing the HBE and OHBE of Ni, Pd–Ni, and Pd_2–Ni displayed in Figure 4a (HBE–Ni: −0.357 eV, OHBE–Ni: −0.142 eV; HBE–Pd–Ni: −0.354 eV, OHBE–Pd–Ni: −0.110 eV; HBE-Pd_2–Ni: −0.564 eV OHBE-Pd_2–Ni: −0.212 eV), it is evident that both HBE and OHBE are weakened after the introduction of Pd SA, but are strengthened in the Pd_2–Ni model (Figure 4a). The structural models and corresponding differential charge density diagrams of Pd–Ni and Pd_2–Ni reveal that the insertion of Pd SA and Pd dimer into the Ni lattice induces a significant charge transfer from Ni to Pd at the interface (Figure 4b, Figures S23 and S26), thereby altering the adsorption energy of intermediates.

Additionally, the slightly downward shift of the d-band center between Ni and Pd–Ni (−1.94 *vs* −1.95 eV) might also assist in modulating the HBE, as the lower energy level of the d-band center implies a weaker affinity of the catalyst to hydrogen species (Figure S24). Subsequently, the free energy profiles for the alkaline HOR process on Ni, Pd–Ni, and Pd_2–Ni were calculated. As illustrated in Figure 4c, the combination of H* and OH* to regenerate H_2O (Volmer step) is the rate-determining step (RDS) for HOR on all three catalysts due to the relatively high energy barrier. Interestingly, the reaction energy for the RDS (ΔG_{RDS} = 0.52 eV) on Pd–Ni is nearly identical to that on Ni (0.51 eV), while the activation barrier (E_a) for water formation on Pd–Ni (E_a = 1.02 eV) is much lower than that Ni (1.57 eV). For Pd_2–Ni, the ΔG_{RDS} and E_a were calculated to be 0.50 and 1.01 eV, respectively. The correlation between ΔG_{RDS} and E_a for Pd–Ni or Pd_2–Ni deviates from the typical BEP relation in heterogeneous catalysis, which can be attributed to the decoupling of reactants dissociation and intermediates binding in SAAs or dilute alloys.[26] Specifically, H_2 molecules dissociated at a more reactive Pd SA/dimer site and intermediates (H*/OH*) bind at the surrounding less active Ni. In 2015, Zitoun et al. constructed a series of Pd/Ni electrodes (electrolytic deposition of Pd onto Ni surfaces) with different Pd coverage from 1 % to 80 %, and then performed a systematic study to clarify the relationship between Pd coverage and HOR performance in alkaline media.[27] They found that the current density linearly increased with the Pd coverage up to 17 %, but further increase resulted in a plateau of HOR activity. Since the surface composition of Pd/Ni would be islands of Pd atoms (instead of Pd SAs) on Ni without alloying, this surface segregation seems much less prone to electronic effects, and the role of Ni could be related to its exophilic character. The comparison of 0.5 % Pd–Ni with Pd/Ni further highlights the great potential of dilute alloys in enhancing HOR performance by breaking the linear scaling relationships and reducing cost by maximizing atom efficiency.

Conclusion

In summary, a dilute Pd–Ni alloy catalyst has been rationally designed and efficiently fabricated to enhance the HOR in alkaline media. As verified by HAADF-STEM and EXAFS analyses, Pd atoms were precisely anchored in the lattice of the Ni substrate through the pyrolysis of a trace-Pd decorated NiC_2O_4-CP precursor. The resulting 0.5 % Pd–Ni catalyst demonstrates outstanding HOR performances in 0.1 M KOH, with an exchange current density and mass activity of 0.055 mA cm^{-2} ($j^{0,s}$) and 4.275 mA mg$^{-1}_{metal}$ ($j^{0,m}$), respectively, which are comparable to those of many benchmark HOR catalysts. Furthermore, theoretical calculations reveal the regulating effect of Pd SA/dimer on the electronic structure of reactive sites, which contributes to enhanced HOR activity by optimizing the HBE/OHBE and lowering the activation energy barrier of water generation (RDS). This work not only underscores the synergetic effect between bimetallic atoms within dilute alloy catalysts for alkaline HOR, but also provides valuable guidance for designing and synthesizing advanced electrocatalysts toward energy conversion with maximum atomic efficiency.

Acknowledgements

The authors gratefully acknowledge the financial support from the National Natural Science Foundation of China (22371165, 21971143), the 111 Project (D20015), the project of Hubei Three Gorges Laboratory (Z2022078, SK213002), the postdoctoral innovation research foundation of Hubei Province (287189), and the NSF of Hubei Province (2020CFB686).

Conflict of Interest

The authors declare no conflict of interest.

Data Availability Statement

The data that support the findings of this study are available from the corresponding author upon reasonable request.

Keywords: Fuel cells · alkaline hydrogen oxidation reaction · coordination polymer · dilute Pd–Ni alloy

[1] a) W. Ni, T. Wang, F. Héroguel, A. Krammer, S. Lee, L. Yao, A. Schüler, J. S. Luterbacher, Y. Yan, X. Hu, *Nat. Mater.* **2022**, *21*, 804–810; b) Y. Xue, L. Shi, X. Liu, J. Fang, X. Wang, B. P. Setzler, W. Zhu, Y. Yan, Z. Zhuang, *Nat. Commun.* **2020**, *11*, 5651; c) N. Ramaswamy, S. Mukerjee, *Chem. Rev.* **2019**, *119*, 11945–11979.

[2] a) J. Zhang, W. Zhu, T. Huang, C. Zheng, Y. Pei, G. Shen, Z. Nie, D. Xiao, Y. Yin, M. D. Guiver, *Adv. Sci.* **2021**, *8*, 2100284; b) J. C. Douglin, J. A. Zamora Zeledón, M. E. Kreider, R. K. Singh, M. B. Stevens, T. F. Jaramillo, D. R. Dekel, *Nat. Energy.* **2023**, *8*, 1262–1272.

[3] a) Y. Cong, B. Yi, Y. Song, *Nano Energy.* **2018**, *44*, 288–303; b) X. Zhang, L. Xia, G. Zhao, B. Zhang, Y. Chen, J. Chen, M. Gao, Y. Jiang, Y. Liu, H. Pan, W. Sun, *Adv. Mater.* **2023**, *35*, 2208821; c) L. Su, D. Gong, Y. Jin, D. Wu, W. Luo, *J. Energy Chem.* **2022**, *66*, 107–122.

[4] Z.-C. Yao, T. Tang, Z. Jiang, L. Wang, J.-S. Hu, L.-J. Wan, *ACS Nano* **2022**, *16*, 5153–5183.

[5] a) L. An, X. Zhao, T. Zhao, D. Wang, *Energy Environ. Sci.* **2021**, *14*, 2620–2638; b) X. Tian, P. Zhao, W. Sheng, *Adv. Mater.* **2019**, *31*, 1808066; c) Y. H. Wang, X. T. Wang, H. Ze, X. G. Zhang, P. M. Radjenovic, Y. J. Zhang, J. C. Dong, Z. Q. Tian, J. F. Li, *Angew. Chem. Int. Ed.* **2021**, *60*, 5708–5711; d) M. Ma, G. Li, W. Yan, Z. Wu, Z. Zheng, X. Zhang, Q. Wang, G. Du, D. Liu, Z. Xie, Q. Kuang, L. Zheng, *Adv. Energy Mater.* **2022**, *12*, 2103336.

[6] a) N. Alonso-Vante, *Electrochem. Energy Rev.* **2023**, *6*, 3; b) X. Mu, S. Liu, L. Chen, S. Mu, *Small Struct.* **2023**, *4*, 2200281.

[7] C. Zhan, Y. Xu, L. Bu, H. Zhu, Y. Feng, T. Yang, Y. Zhang, Z. Yang, B. Huang, Q. Shao, X. Huang, *Nat. Commun.* **2021**, *12*, 6261.

[8] Z. Qiu, Y. Li, Y. Gao, Z. Meng, Y. Sun, Y. Bai, N. T. Suen, H. C. Chen, Y. Pi, H. Pang, *Angew. Chem. Int. Ed.* **2023**, *62*, e202306881.

[9] a) K. Wang, J. Huang, H. Chen, Y. Wang, W. Yan, X. Yuan, S. Song, J. Zhang, X. Sun, *Electrochem. Energy Rev.* **2022**, *5*, 17; b) L. Zhao, H. Liu, Y. Liu, X. Han, J. Xu, W. Xing, W. Guo, *ACS Appl. Mater. Interfaces* **2020**, *12*, 40248–40260; c) R. Zhao, X. Yue, Q. Li, G. Fu, J. M. Lee, S. Huang, *Small* **2021**, *17*, 2100391; d) L. Lu, L. Peng, L. Li, J. Li, X. Huang, Z. Wei, *J. Energy Chem.* **2020**, *40*, 52–56; e) B. Pang, C. Jia, S. Wang, T. Liu, T. Ding, X. Liu, D. Liu, L. Cao, M. Zhu, C. Liang, Y. Wu, Z. Liao, J. Jiang, T. Yao, *Nano Lett.* **2023**, *23*, 3826–3834.

[10] a) X. Li, Z. Guo, J. Yang, Y. Li, X. Sun, H. He, S. Li, J. Zhang, *Electrochem. Energy Rev.* **2022**, *5*, 9; b) W. Guo, Z. Wang, X. Wang, Y. Wu, *Adv. Mater.* **2021**, *33*, 2004287; c) J. Yang, W. Li, D. Wang, Y. Li, *Adv. Mater.* **2020**, *32*, 2003300; d) T. Zhang, A. G. Walsh, J. Yu, P. Zhang, *Chem. Soc. Rev.* **2021**, *50*, 569–588; e) T. Shen, S. Wang, T. Zhao, Y. Hu, D. Wang, *Adv. Energy Mater.* **2022**, *12*, 2201823.

[11] R. T. Hannagan, G. Giannakakis, M. Flytzani-Stephanopoulos, E. C. H. Sykes, *Chem. Rev.* **2020**, *120*, 12044–12088.

[12] R. Wan, M. Luo, J. Wen, S. Liu, X. Kang, Y. Tian, *J. Energy Chem.* **2022**, *69*, 44–53.

[13] X. Cheng, Y. Wang, Y. Lu, L. Zheng, S. Sun, H. Li, G. Chen, J. Zhang, *Appl. Catal. B* **2022**, *306*, 121029.

[14] A. R. Poerwoprajitno, L. Gloag, J. Watt, S. Cheong, X. Tan, H. Lei, H. A. Tahini, A. Henson, B. Subhash, N. M. Bedford, B. K. Miller, P. B. O'Mara, T. M. Benedetti, D. L. Huber, W. Zhang, S. C. Smith, J. J. Gooding, W. Schuhmann, R. D. Tilley, *Nat. Catal.* **2022**, *5*, 231–237.

[15] J. Mao, C.-T. He, J. Pei, Y. Liu, J. Li, W. Chen, D. He, D. Wang, Y. Li, *Nano Lett.* **2020**, *20*, 3442–3448.

[16] X. Wang, Y. Tong, W. Feng, P. Liu, X. Li, Y. Cui, T. Cai, L. Zhao, Q. Xue, Z. Yan, X. Yuan, W. Xing, *Nat. Commun.* **2023**, *14*, 3767.

[17] L. Chen, X. Liang, D. Wang, Z. Yang, C.-T. He, W. Zhao, J. Pei, Y. Xue, *ACS Appl. Mater. Interfaces* **2022**, *14*, 27814–27822.

[18] T. Zhao, G. Wang, M. Gong, D. Xiao, Y. Chen, T. Shen, Y. Lu, J. Zhang, H. Xin, Q. Li, D. Wang, *ACS Catal.* **2020**, *10*, 15207–15216.

[19] A. N. Puzan, V. N. Baumer, D. V. Lisovytskiy, P. V. Mateychenko, *J. Solid State Chem.* **2018**, *266*, 133–142.

[20] H. Wang, Q. Luo, W. Liu, Y. Lin, Q. Guan, X. Zheng, H. Pan, J. Zhu, Z. Sun, S. Wei, J. Yang, J. Lu, *Nat. Commun.* **2019**, *10*, 4998.

[21] N. Marcella, J. S. Lim, A. M. Plonka, G. Yan, G. J. Owen, J. E. S. van der Hoeven, A. C. Foucher, H. T. Ngan, S. B. Torrisi, N. S. Marinkovic, E. A. Stach, J. F. Weaver, J. Aizenberg, P. Sautet, B. Kozinsky, A. I. Frenkel, *Nat. Commun.* **2022**, *13*, 832.

[22] M. Luneau, E. Guan, W. Chen, A. C. Foucher, N. Marcella, T. Shirman, D. M. A. Verbart, J. Aizenberg, M. Aizenberg, E. A. Stach, R. J. Madix, A. I. Frenkel, C. M. Friend, *Commun. Chem.* **2020**, *3*, 46.

[23] K. Mori, T. Hara, T. Mizugaki, K. Ebitani, K. Kaneda, *J. Am. Chem. Soc.* **2004**, *126*, 10657–10666.

[24] a) P. Aich, H. Wei, B. Basan, A. J. Kropf, N. M. Schweitzer, C. L. Marshall, J. T. Miller, R. Meyer, *J. Phys. Chem. C* **2015**, *119*, 18140–18148; b) F. R. Lucci, J. Liu, M. D. Marcinkowski, M. Yang, L. F. Allard, M. Flytzani-Stephanopoulos, E. C. H. Sykes, *Nat. Commun.* **2015**, *6*, 8550.

[25] a) K. I. Hadjiivanov, G. N. Vayssilov, *Adv. Catal.* **2002**, *47*, 307; b) M. Ouyang, K. G. Papanikolaou, A. Boubnov, A. S. Hoffman, G. Giannakakis, S. R. Bare, M. Stamatakis, M. Flytzani-Stephanopoulos, E. C. H. Sykes, *Nat. Commun.* **2021**, *12*, 1549.

[26] M. T. Darby, M. Stamatakis, A. Michaelides, E. C. H. Sykes, *J. Phys. Chem. Lett.* **2018**, *9*, 5636–5646.

[27] I. Bakos, A. Paszternák, D. Zitoun, *Electrochim. Acta* **2015**, *176*, 1074–1082.

Manuscript received: July 5, 2024
Accepted manuscript online: August 21, 2024
Version of record online: ■■, ■■

Research Article

Electrocatalytic H_2 Oxidation

Y. Yuan, X.-Q. Wu,* X. Yin, H.-Y. Ruan, Y.-P. Wu, S. Li, G. Hai, G. Zhang, S. Sun,* D.-S. Li* **e202412680**

Dilute Pd–Ni Alloy through Low-temperature Pyrolysis for Enhanced Electrocatalytic Hydrogen Oxidation

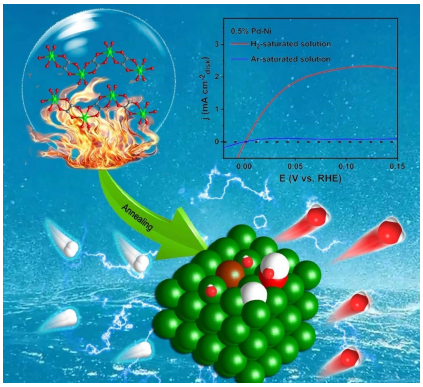

A highly efficient dilute Pd–Ni alloy HOR electrocatalyst has been developed from a Pd-doped Ni-based coordination polymer through low-temperature pyrolysis. This work offers new perspectives for designing more advanced electrocatalysts for energy conversion.